APL Materials

RESEARCH ARTICLE | MAY 08 2025

Metal interdiffusion enhanced WO_x/CuO_x heterojunction optoelectronic memristive synapses for face recognition application

Special Collection: Energy-Efficient Memory Materials

Hans Juliano ; Stephen Ekaputra Limantoro ; Firman M. Simanjuntak ; Tseung-Yuen Tseng

APL Mater. 13, 051112 (2025)
https://doi.org/10.1063/5.0252709

View Online

Export Citation

Articles You May Be Interested In

Efficient control of magnetization dynamics via W/CuO_X interface

Appl. Phys. Lett. (September 2024)

High-photoresponse mixed-dimensional CuO_x/WSe_2 p-type phototransistor with van der Waals interface

Appl. Phys. Rev. (April 2025)

Bipolar resistance switching in $Pt/CuO_x/Pt$ via local electrochemical reduction

Appl. Phys. Lett. (June 2014)

02 July 2025 08:13:56

Metal interdiffusion enhanced WO_x/CuO_x heterojunction optoelectronic memristive synapses for face recognition application

Cite as: APL Mater. 13, 051112 (2025); doi: 10.1063/5.0252709
Submitted: 11 December 2024 • Accepted: 24 April 2025 •
Published Online: 8 May 2025 • Corrected: 16 May 2025

Hans Juliano,[1] Stephen Ekaputra Limantoro,[1] Firman M. Simanjuntak,[2,a)] and Tseung-Yuen Tseng[3,a)]

AFFILIATIONS

[1] Department of Electrical Engineering and Computer Science, National Yang Ming Chiao Tung University (NYCU), Hsinchu 30010, Taiwan
[2] School of Electronics and Computer Science, University of Southampton, Southampton S017 1BJ, United Kingdom
[3] Institute of Electronics, National Yang Ming Chiao Tung University (NYCU), Hsinchu 30010, Taiwan

Note: This paper is part of the Joint Special Topic on Energy-Efficient Memory Materials from APL Materials and APL Energy.
[a)] **Authors to whom correspondence should be addressed:** f.m.simanjuntak@soton.ac.uk and tseng@cc.nctu.edu.tw

ABSTRACT

Annealing improves the switching and synaptic performance of ITO/WO_x/CuO_x/ITO transparent devices. The device has low SET and RESET voltages, stable and robust AC endurance of up to 10^6 cycles, and can retain the states for more than 10^4 s. The device demonstrates synaptic capabilities by emulating neural functions under both electrical and light stimuli. The behaviors including long-term potentiation/depression, paired-pulse facilitation, spike-timing-dependent plasticity, and fully tunable relaxation time of short-term memory, mimicking the temporal dynamics of the biological neuron, are declared. A convolutional neural network operation is conducted by exploiting the synaptic functions of the device. The high accuracy of 96.67% with high noise tolerance (close to an ideal synapse) can be achieved. Material analyses are conducted, and switching/synaptic mechanisms are proposed to explain such phenomena.

© 2025 Author(s). All article content, except where otherwise noted, is licensed under a Creative Commons Attribution (CC BY) license (https://creativecommons.org/licenses/by/4.0/). https://doi.org/10.1063/5.0252709

02 July 2025 08:13:56

The increasing demand for neuromorphic computing and making more energy-efficient and high-performance computing hardware has driven extensive research into developing synaptic devices that can mimic biological synaptic behaviors.[1,2] Optoelectronic memristive synapses have become a promising candidate for neuromorphic hardware due to their ability to integrate the benefits of both photonic and electronic systems, thereby enhancing the speed and efficiency of neuromorphic computing.[3] Recent reports suggest that memristive devices made of p–n junction films have better performance than single-layer devices made of either p- or n-type films.[4–6] P- and n-type films have unique defect type and concentration that govern the electron conduction in the films. Stacking such two types of films could avoid random formation and rupture of conducting filaments in memristive cells, thus enhancing the electrical performance.[7] However, those reports did not investigate whether the devices can still perform well after they are subjected to an annealing process. The CMOS compatibility of memristive devices should be tested to determine if the devices can "survive" at back-end-of-line (BEOL) annealing temperature.[5,8–10] In this study, we investigate the impact of annealing on the performance of memristive devices fabricated by WO_x/CuO_x p–n films sandwiched between ITO electrodes. We observed that the annealed devices demonstrated better performance than the as-deposited ones. Device reliability and versatility to be varied by light and electrical stimuli were also observed and studied. Materials analyses were also conducted to explain the performance enhancement of the devices after annealing.[11]

Commercial indium tin oxide (ITO) coated glass substrates were cleaned with acetone and propanol in an ultrasonic cleaner and dried with nitrogen gas. The resistive layers consisting of 10 nm CuO_x and 40 nm WO_x were sequentially deposited using a 50 W RF sputtering system under 10 mTorr argon at room temperature,

© Author(s) 2025

employing CuO_x and WO_x targets, respectively. Thereafter, post-deposition annealing was conducted at 300 °C for 30 min. in a vacuum ambient. This annealing condition was chosen due to the typical annealing in the BEOL process.[5,9] Finally, 100 nm ITO top electrodes (TEs) with a diameter of 150 μm were deposited via RF sputtering using a metal shadow mask, and the schematic of the ITO/WO_x/CuO_x/ITO p–n heterojunction memristive device is shown in Fig. 1(a). The UV–Vis transmittance spectrum, shown in Fig. 1(b) and its inset, demonstrates the device transparency, with a 90% transmittance in visible light. The thickness and compositional identification of layers were confirmed using a transmission electron microscope (TEM) and energy-dispersive spectroscopy (EDS, Thermo Fisher Scientific Spectra 300); the results are depicted in Figs. 1(c) and 1(d), respectively. The thicknesses of WO_x and CuO_x are found to be 40 and 10 nm, respectively, and elemental composition is confirmed by the EDS line scan. As-deposited and as-annealed devices are denoted as AD and AA devices, respectively. Electrical characterization was conducted using an Agilent B1500A semiconductor parameter analyzer and an Agilent B1530A waveform generator, while optical stimuli were applied via a violet laser source (wavelength of 405 nm with a power density of 120 mW/mm^2); a voltage bias was applied to the top electrode while the bottom electrode was grounded, and current compliance (CC) was used to avoid device breakdown. Surface morphology was studied using scanning electron microscopy (SEM, Hitachi SU-8010) and atomic force microscopy (AFM, Veeco Dimension-3100). X-ray photoelectron spectroscopy (XPS, Thermo Fisher Scientific ESCALAB Xi+) was used to analyze defect concentration and elemental distribution in the multilayer films.

Typical I–V sweeping curves for the AD and AA devices are shown in Fig. 2(a). In the low voltage region, the AD device exhibits rectifying behavior, confirming its p–n heterojunction; however, the annealing process suppresses the diode characteristic [inset of Fig. 2(a)]. A negative voltage sweeps the devices from a high resistance state (HRS) to a low resistance state (LRS) (SET process); note that the devices are forming-free. Conversely, a positive sweep switches the devices from LRS to HRS (RESET process). The annealing treatment not only reduces the current compliance (CC) required to switch the devices but also decreases the SET (from −1.4 to −1 V, Vset) and RESET voltages (from 2.0 to 1.2 V, Vreset). The AA device exhibits better endurance, demonstrating stable switching cycles with a memory window of 37 without any data errors or state decay for over 1200 cycles. Note that we conducted annealing at various temperatures and found that annealing temperatures below and above 300 °C deteriorate the performance of the device. We suggest that this phenomenon is due to the trade-off between the

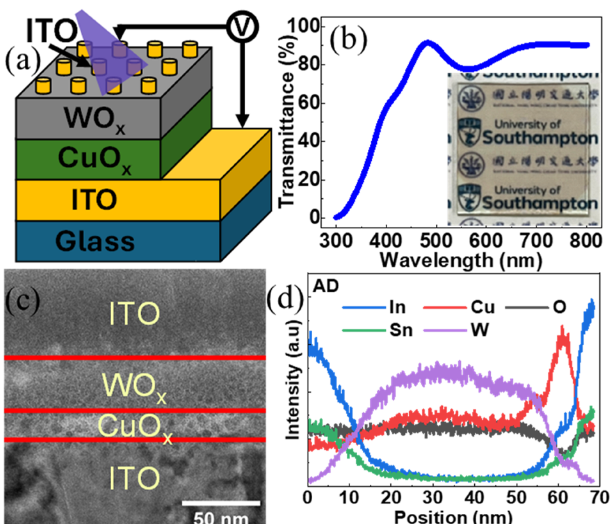

FIG. 1. (a) Schematic diagram of the ITO/WO_x/CuO_x/ITO device under violet light illumination. (b) Transmittance spectra of the memristor device; the inset highlights the excellent transparency of the memristor device. (c) Cross-sectional TEM and (d) EDS line scan of the memristive device.

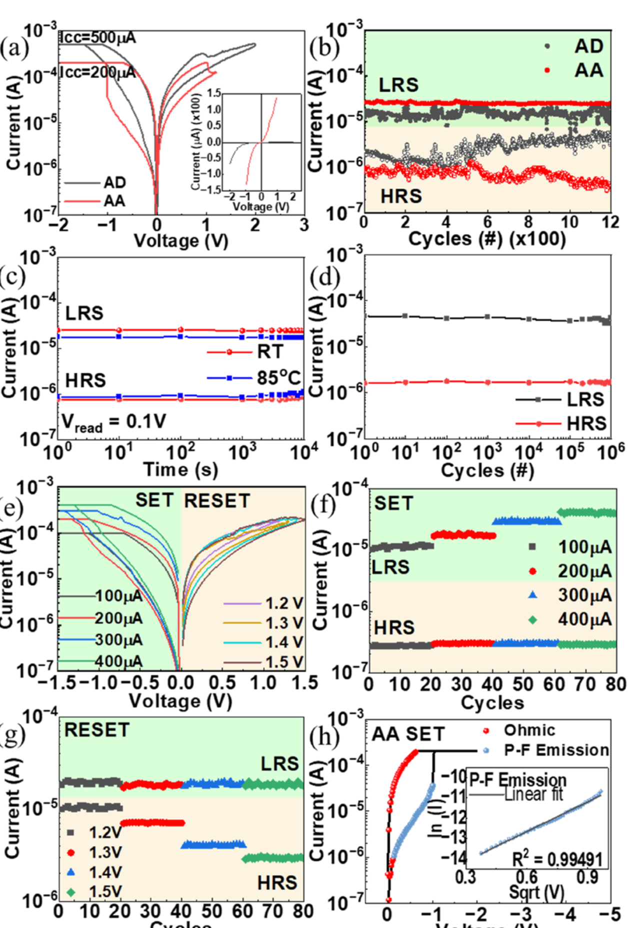

FIG. 2. (a) Typical I–V switching curves of the first cycle of AD and AA devices, with an inset showing the I–V scan in the pristine condition for the devices. (b) Endurance characteristics of AD and AA devices over multiple switching cycles. (c) Retention performance of AA in both resistance states at RT and 85 °C. (d) Endurance of the AA device under AC stress (SET: −1.4 V for 300 ns, RESET: 1 V for 100 ns). (e)–(g) Multi-level switching characteristics of the AA device. (h) Conduction mechanism fitting for the AA device, with the inset showing the details of the fittings.

02 July 2025 08:13:56

© Author(s) 2025

crystallinity and lattice mismatch at the interfaces (see Fig. S1 of the supplementary material for details).[12,13]

Based on the above results, it is clear that the AA device works at lower voltage and current and has better stability, which is more appealing for low-power system implementation. It is found that the AA device is capable of retaining its HRS and LRS for more than 10^4 s at an elevated temperature and performing robust AC endurance for more than 10^6 cycles, as depicted in Figs. 2(c) and 2(d). Figures 2(e)–2(g) show that the device can be programmed to demonstrate multi-state characteristics by varying the CC and RESET voltages; a 2-bits/cell storage operation can be achieved, indicating its capability for high-density data storage. The switching process is governed by the Ohmic law in the low voltage region of HRS, suggesting that injected carriers may initially encounter resistance due to traps or interfacial barriers.[14] At higher voltages in the HRS and LRS, the conduction mechanism transitions to Poole–Frenkel (P–F) as depicted in Fig. 2(h), indicating the presence of the amount and kind of defects determining the switching properties of the device.

Figure 3(a) exhibits the long-term potentiation (LTP) and depression (LTD) of the devices. It is found that the AA device exhibits more stable epoch training than the AD device; moreover, the AA device has lower noise and a larger dynamic range of 140%. This further confirms that the AA device is superior to AD. Figure 3(b) shows that the AA device has minimal deviation in the maximum and minimum conductance states (G_{max} and G_{min}) during the 500 epochs, where the symmetric error is small. The method of the symmetric error calculation is explained in our previous work.[15] This high level of symmetry could positively impact brain-inspired computation.[16] The LTP/LTD curves are well-fitted using the following equations to determine their nonlinearity (NL) values:[17]

$$G_{LTP} = B\left(1 - \exp^{\left(-\frac{P}{A}\right)}\right) + G_{\min}, \tag{1}$$

$$G_{LTD} = -B\left(1 - \exp^{\left(-\frac{P-P_{\max}}{A}\right)}\right) + G_{\max}, \tag{2}$$

$$B = \frac{G_{\max} - G_{\min}}{1 - \exp^{\left(-\frac{P_{\max}}{A}\right)}}, \tag{3}$$

where P_{max} is the maximum spike number, and the nonlinearity (NL) is fitted by using parameter B, functioning as a parameter of A, which reflects the behavior of the system.[18] It is found that the NL is less than three [Fig. 3(c)], indicating that the LTP/LTD performance could be useful for efficient neuromorphic computation.[19]

Figure 3(d) shows the spike-timing-dependent plasticity (STDP) capabilities of the device. The spike time difference (Δt) represents the interval between the presynaptic and postsynaptic pulses, calculated as $\Delta t = t_{pre} - t_{post}$. The conductance change was measured

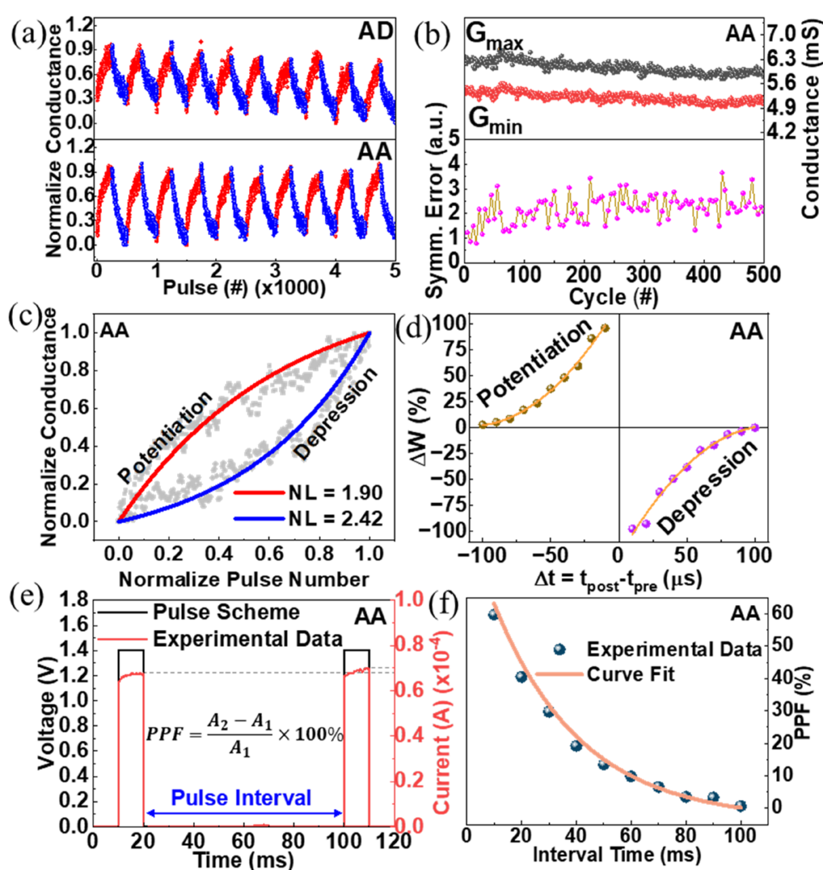

FIG. 3. (a) Ten epochs of LTP and LTD of AD and AA devices; amplitude −1.2 and 1.4 V with a pulse width of 10 μs and a read pulse of 0.1 V, 1 ms. (b) Fitting curve showing NL coefficients for both potentiation and depression. (c) G_{max} and G_{min} values over a total of 500 cycles, along with symmetric error analysis of 100 randomly selected LTP/LTD cycles. (d) Asymmetric anti-Hebbian STDP response of the device for time intervals Δt < 0 and Δt > 0; the pulse width of each short spike is maintained at 100 μs with pulse heights of +1.4 and −1.4 V. (e) Applied voltage bias of electrical spikes for PPF and corresponding measured current. (f) Electrical PPF index.

02 July 2025 08:13:56

© Author(s) 2025

as a function of Δt, with presynaptic and postsynaptic pulses applied accordingly. The change in conductance (ΔG) was calculated using the formula $\Delta G = (G_2 - G_1)/G_1$, where G_1 and G_2 are the conductance states before and after the pulse sequence, respectively. This variation in conductance states follows an exponential relationship with synaptic weight, as described by the following function:[20]

$$\Delta G = \begin{cases} A_1 \exp\left(-\dfrac{\Delta t}{\tau_1}\right), \Delta t > 0, \\ A_2 \exp\left(-\dfrac{\Delta t}{\tau_2}\right), \Delta t < 0, \end{cases} \quad (4)$$

where A_1 and A_2 are the scaling factors, whereas τ_1 and τ_2 are time constants. The results show that the AA device reveals an asymmetric anti-Hebbian STDP response, with potentiation (P) and depression (D) observed in the second and fourth quadrants. The conductance change is inversely proportional to the time difference between spikes, closely responding biological synapse behavior and supporting the potential for neural applications.[21]

PPF is another essential synaptic function, exhibiting changes in synaptic weight following multiple excitatory postsynaptic potentials.[22] We evaluate the PPF by applying two identical spikes with varying time intervals, and the corresponding ΔG is measured, as shown in Fig. 3(e). Measurements are taken after fully resetting the device to HRS to ensure accurate current responses for each test. The conductance change between the two spikes is used to calculate the PPF index based on the formula provided in the inset of Fig. 3(e). Curve fitting as indicated in Fig. 3(f) is performed using the following equation:[23]

$$PPF = C1 \times \exp\left(\frac{-t}{\tau_1}\right) + C2 \times \exp\left(\frac{-t}{\tau_2}\right), \quad (5)$$

where t is the duration between two spikes, C1 and C2 are the starting magnitudes of the phases, and τ_1 and τ_2 are the relaxation times for the rapid and slow phases, respectively. It is found that $\tau_1 = 31.548$ s and $\tau_2 = 31.544$ s. This demonstrates that the AA device has the ability to emulate PPF that could enable realistic short-term memorization stimulation for neuromorphic computing.[24] The above results show that the switching and synaptic performance of the AA device is better than that of the AD device. Materials analysis was conducted to elucidate this phenomenon.

The SEM images [Fig. 4(a)] illustrate that annealing increases the grain size and crystalline quality; meanwhile, the AFM topography [insets of Fig. 4(a)] reveals that the annealed film has lower surface roughness with fewer grain boundaries and micro-voids. This denser structure facilitates less formation of conduction filament branches along the grain boundaries.[10] XPS depth profile analyses shown in Fig. 4(b) reveal that the annealing process induces metal interdiffusion at the interfaces to cause a high concentration of In atoms at the TE/WO_x and CuO_x/bottom electrode (BE) interfaces, while the Cu diffuses into the WO_x film. Indium (In) and cupper (Cu) atoms are known to diffuse relatively easily into adjacent layers under thermal treatment.[25,26] The annealing process also increases the oxygen vacancy (Vo) concentration in the annealed films, as depicted in Fig. 4(c);[25] the XPS O1s spectra analysis was performed by following methods reported in the literature.[27] The diffused metallic defects and oxygen vacancies alter the property of interfacial layers. Based on the above materials analysis, we can explain the switching and synaptic mechanism of the devices as depicted in the schematic shown in Fig. 4(d).

Since the AD device has less number of oxygen vacancies (Vo) that are distributed within the WO_x and CuO_x layers, and the indium atoms (In) are diffused predominantly at the top and

02 July 2025 08:13:56

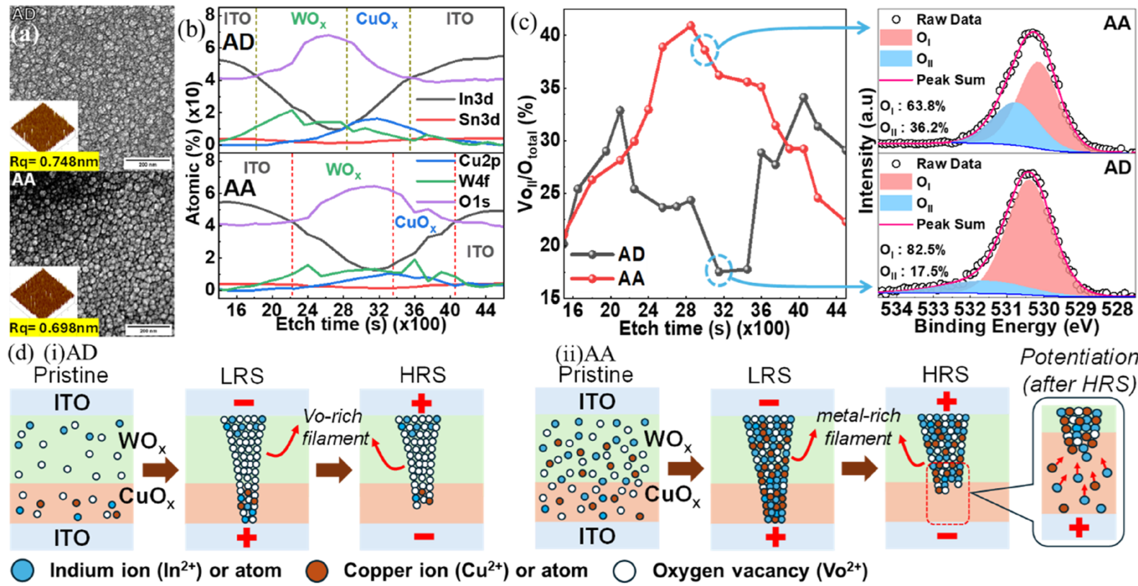

FIG. 4. (a) Surface scan micrographs of AD and AA films, with inset AFM images showing surface topography and root mean square (Rq) roughness values. (b) XPS depth profile spectra of the AD and AA devices, respectively. (c) Vo concentration at different depths for AD and AA devices and the typical O1s spectra and their fitting near the WO_x/CuO_x interface. (d) Schematic illustration of the switching mechanism for (i) AD and (ii) AA devices.

© Author(s) 2025

bottom electrode interfaces [Figs. 4(b) and 4(c)], a negative bias to the TE will create new Vo^{2+} defects by ionizing oxygens in the WO_x and CuO_x layers and simultaneously ionize indium atoms (In^{3+} cations) and thereafter repulse positively charge defects (In^{3+} and Vo^{2+} toward TE). From the TE interface, the filament grows, reaching BE, where the filament will consist of Vo and In, connecting the TE and BE and switching the device to the LRS state. Note that the pre-existing Vo concentration in the AD is not sufficient to complete filamentary formation, which is why a creation of Vo is required and a higher Vset is observed in the AD device [Fig. 2(a)]. When the polarity is reversed, oxygen ions from the BE interface will recombine with the Vo, and the In will drift back to the BE, causing the filament to rupture within the CuO_x layer and return the device to HRS. Meanwhile, in the AA device, the annealing introduces extensive diffusion of In and copper (Cu) atoms toward the WO_x layer, and thus, a higher number of Vo, In, and Cu defects exist in the pristine state, as compared to the AD device. These accumulated defects at the interface reduce the barrier height of the p–n junction, thereby weakening the rectifying behavior and suppressing the diode-like effect. This observation is further supported by the temperature coefficient of resistance,[28] TCR, $\alpha(AA) = 0.0049\,^{\circ}C^{-1}$, which is consistent with values typically associated with composite filament-based devices.[29] This positive TCR behavior indicates that the low-resistance state conduction is not governed by interfacial effects but rather by metallic or semi-metallic filaments formed via the diffusion of indium and copper ions. A positive bias drifts Cu^{2+}, In^{3+}, and Vo^{2+} defects toward the TE during the SET process. Since the concentration of In is high at the region near the BE and TE interfaces, while a high number of Vo and Cu are distributed in the WO_x region, the base and the body of the filament will consist of the mixture of In, Cu, and Vo defects. Meanwhile, the apex of the filament will predominantly consist of In and Cu atoms. The availability of sufficient defects in the pristine state makes the formation of filament easy, and the size of the filament is a bit bigger than that of the AD device; thus, the AA device has a lower Vset and higher LRS current [Figs. 2(a) and 2(b)], respectively.[30] Metal cations have lower ionization energy (Cu = 7.726 eV, In = 5.786 eV, and O = 13.618 eV)[31] and migrate faster than oxygen atoms, causing the filament to rupture easily and resulting in a larger gap between the ruptured filament and the electrode during the RESET process;[32] thus, the AA device requires a lower Vreset and a larger memory window. Moreover, the lower number of grain boundaries in the annealed films helps reduce the formation of branch filaments. We suspect that the switching instability of the AD device is due to the generation of stronger branches at the grain boundaries after repeated switching cycles that lead to a high fluctuation and the decay of the memory window [Fig. 2(b)].

P and D have processes similar to those of the LRS and HRS; however, the redox reaction and defect migration occur in short pulses. The P is performed after resetting the device (HRS), and short negative pulses (−1.2 V) repulse cation metals from BE toward the ruptured filament, gradually increasing the conductance (synaptic weight) of the cell; note that P does not rejuvenate the filament back to LRS since the energy that is given by the short pulses is not as high as the SET process. The device requires a slightly higher D pulse amplitude (+1.4 V); this is because the holes that are injected from the TE need to travel a large distance across the body toward the tip of the metal filament; meanwhile, the injection of electrons from the BE is more difficult due to the large gap between the BE and the tip of the filament, and the metal cations need to cross this gap to depress the filament.

Our device responds to light illumination, as shown in Fig. 5(a). The photogenerated current (I_p) increases steadily during the 600 s of illumination, and the device undergoes an initial rapid current decay [inset of Fig. 5(a)], followed by a much slower, prolonged decay lasting ~20 times the illumination period. This behavior mimics the forgetting mechanism in biological synapse; we further analyze this by employing the Ebbinghaus forgetting curve.[33] As illustrated in Fig. 5(b), the relaxation data extracted from Fig. 5(a) are fitted using a double exponential decay model, as described by Eq. (5). The calculated relaxation times are $\tau_1 = 29.246$ s for the fast decay phase and $\tau_2 = 10\,255.221$ s for the slow decay phase, indicating the presence of long-lasting persistent photoconductivity

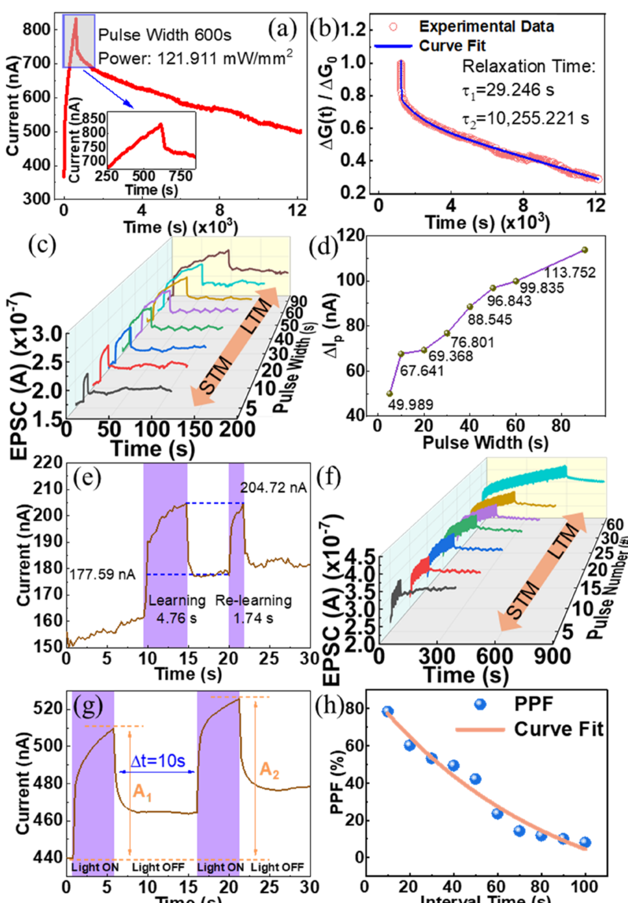

FIG. 5. Programming via light stimulation. (a) Photoresponse under 600 s of illumination, with the inset showing an abrupt change followed by gradual relaxation in darkness over 12 000 s; a constant read voltage of 0.1 V was used. (b) Ebbinghaus forgetting curve following 600 s illumination [extracted from (a)] showing the decay. (c) STM to LTM transition under varying pulse widths. (d) Photocurrent change as a function of pulse width [extracted from (c)]. (e) Learning and re-learning behavior. (f) STM to LTM transition observed under varying numbers of illumination pulses. (g) Optical PPF with two identical stimulation pulses. (h) PPF index variation with interval time between optical pulses.

02 July 2025 08:13:56

© Author(s) 2025

(PPC) in the device;[15] see Fig. S2 of the supplementary material, for the detailed explanation of the carrier recombination and trapping dynamics during the decay phases. This programming and forgetting process can be finely tuned by changing the optical stimulation parameters. As shown in Fig. 5(c), I_p increases with the duration of the optical spikes (ranging from 5 to 90 s), with wider spikes producing a more significant change in I_p (ΔI_p). This correlation between the spike width and I_p change is further illustrated in Fig. 5(d), where the trend of ΔI_p indicates that the decay process slows down as the spike width increases, demonstrating the learning behavior observed in the human brain, where longer stimuli reinforce memory retention, allowing a transition from short-term to long-term memorization (STM-to-LTM).[18] This result is also consistent with previously reported findings,[34] further supporting the memristor's ability to emulate biological memory processes.

In the human brain, the re-learning process for forgotten information typically requires less time than the initial learning.[35] This behavior can be emulated by our device, as shown in Fig. 5(e). Initially, the device is illuminated by an optical spike for 4.76 s, resulting in an increase in I_p to 204.72 nA. After turning off the light source for 5 s, I_p decreases to an intermediate state of 177.59 nA. Upon re-illumination, it takes only 1.74 s for I_p to return to its previous learning level, a shorter time than that required for the initial spike. This re-learning capability demonstrates that our device can simulate memory reinforcement, similar to cognitive learning in biological systems. Based on this, a stimulation number-dependent learning measurement was conducted, and the result is depicted in Fig. 5(f). It is indicated that the device is first exposed to five consecutive light pulses, resulting in excitatory postsynaptic currents (EPSCs) increasing to 349.65 nA before the stimulus is turned off. This result illustrates STM behavior based on temporary retention rather than a complete return to the initial state.[36] Repeated stimulation enables STM to transition into LTM, as evidenced by a more pronounced EPSC increase when the number of pulses is increased (from 10 to 60). This increment in EPSC decays more slowly than the EPSC generated by fewer repetitions, indicating that stronger potentiation effects occur with more extensive stimulation. Consequently, the device demonstrates an STM to LTM transition based on the stimulation frequency, which is in line with the Atkinson and Shiffrin model of cognitive learning.[37] This model suggests that weaker stimuli induce STM, while repeated, stronger stimuli establish LTM. This behavior highlights the device's ability to mimic basic human memory processes and is consistent with previously reported findings.[38]

Similar to the electrical PPF test [Figs. 3(e) and 3(f)], two identical optical pulses at 405 nm with a 5 s width are applied to the device with varying intervals (10–100 s) to emulate PPF synaptic behavior, as shown in Fig. 5(g). The resulting conductance changes, exhibited in Fig. 5(h), are fitted using Eq. (5), yielding relaxation times of τ_1 = 81.784 s and τ_2 = 81.799 s. These findings confirm the device's ability to simulate STM through realistic synaptic responses via light stimuli, supporting its use in optoelectronic applications and neuromorphic computing where both electrical and optical synaptic functions can be employed.[39]

The violet light has a photon energy of about 3.06 eV, while the bandgap of WO_x is 2.7 eV[40] and that of CuO_x is 2.17 eV.[41] Upon illumination, this energy excites electrons in both materials, promoting them from the valence band (E_v) to the conduction band (E_c) and creating electron–hole pairs, thus increasing I_p. When the light illumination is stopped, the slower carrier determines the I_P decay behavior.

To validate the neuromorphic computing feasibility of our device, a convolutional neural network (CNN) is implemented for face recognition by using 32 × 32 $pixel^2$ resized face images from the ORL dataset, as shown in the schematic in Fig. 6(a). The ORL dataset consists of 400 images from 40 different individuals. The images of certain individuals are taken at different times, with varied lighting conditions, face characteristics (e.g., with or without spectacles), and facial attitudes (e.g., smiling or not smiling, open or closed eyes). The subjects are positioned frontally and upright, with room for

02 July 2025 08:13:56

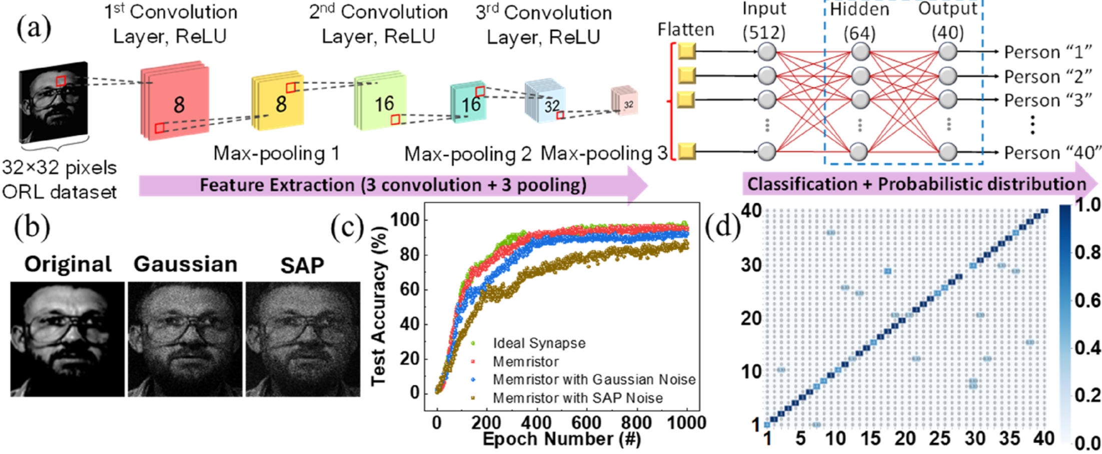

FIG. 6. (a) Schematic diagram of the CNN architecture used in the experiment. (b) Sample ORL face image showing variations in noise levels: original image, Gaussian, and SAP noise. (c) Test accuracy results as a function of epoch number for the CNN under each noise condition. (d) Confusion matrix of 0.10 SAP noise illustrates performance by comparing the desired output classes with their predicted classifications.

© Author(s) 2025

little side movements, in all photographs, which are taken against a uniformly dark background. The CNN architecture includes three convolutional layers, three max-pooling layers, and two fully connected layers. Based on the NL parameter of the device's LTP/LTD characteristics, a backpropagation algorithm is employed to simulate the CNN model, utilizing 280 training images and 120 testing images.

The noise tolerance of the CNN model is assessed by applied Gaussian noise, as salt and pepper[42] each with a 0.10 noise level to the ORL dataset, as shown in Fig. 6(b). After 1000 training epochs, the device achieves an accuracy of 96.67%, compared to 97.75% for an ideal synapse with an NL value of zero. When noise is introduced, the model maintains high accuracy, achieving 93.33% with Gaussian noise and 88.33% with SAP noise. These results, presented in Figs. 6(c) and 6(d), highlight the device's resilience to noise and its potential for accurately classifying corrupted face images, underscoring its suitability for practical neuromorphic computing applications where robustness against noisy data is essential. We also investigated the effect of cycle-to-cycle (C2C) and device-to-device (D2D) variations on the CNN accuracy (see Figs. S3 and S4 of the supplementary material). The C2C analysis showed that the device maintains relatively consistent performance over repeated cycles. Although a slight degradation in nonlinearity (NL) is observed after extended cycling, the LTP/LTD curves and dynamic range remain within acceptable limits for the CNN computation. Meanwhile, the D2D analysis revealed that some fluctuations in device behavior across different cells take randomly in different regions, indicating a variation in the yield and fabrication consistency, which may affect large-scale array integration. However, despite this, the CNN classification accuracy remains high, suggesting that the system is relatively robust to such a variation at the current scale of evaluation.

The metal interdiffusion and enlargement of grains of the films induced by the annealing process on the ITO/WO_x/CuO_x/ITO cell promoted stable switching and synaptic performance. Meanwhile, the device made without annealing suffered from memory window and epoch decay and higher on and off voltages. The metal interdiffusion of In from the electrodes and Cu into the WO_x layer led to the formation of filament predominantly consisting of In and Cu atoms that help the redox process during set/reset and P/D processes. Moreover, the device responded well to light stimuli, demonstrating short-term to long-term memorization. The synaptic function of the device can be used to compute CNN face recognition with high accuracy despite the introduction of noises. This study provides insights into the fabrication of optoelectronic memristive devices for data storage and neuromorphic computing applications.

SUPPLEMENTARY MATERIAL

The supplementary material includes discussions on the effects of annealing at different temperatures, the photoconduction mechanism under violet light illumination, and analyses of cycle-to-cycle and device-to-device variations.

ACKNOWLEDGMENTS

This work was supported by the National Science and Technology Council (NSTC), Taiwan (Project No. 111-2221-E-A49-160-MY3), the UK Royal Society (Grant Nos. IEC\R3\223045-The First Step for U.K.–Taiwan Space Devices Hub and RG\R2\232206-SiMSANeC), and Marie Skłodowska-Curie Actions—European Commission (Grant No. 101029535-MENESIS).

AUTHOR DECLARATIONS

Conflict of Interest

The authors have no conflicts to disclose.

Author Contributions

Hans Juliano: Conceptualization (equal); Data curation (equal); Formal analysis (equal); Investigation (equal); Writing – original draft (equal). **Stephen Ekaputra Limantoro**: Conceptualization (equal); Data curation (equal); Formal analysis (equal); Investigation (equal); Resources (equal); Validation (equal); Writing – review & editing (equal). **Firman M. Simanjuntak**: Formal analysis (equal); Investigation (equal); Methodology (equal); Writing – review & editing (equal). **Tseung-Yuen Tseng**: Funding acquisition (equal); Methodology (equal); Project administration (equal); Supervision (equal); Validation (equal); Writing – review & editing (equal).

DATA AVAILABILITY

The data that support the findings of this study are available from the corresponding authors upon reasonable request.

REFERENCES

[1] V. Erokhin, "Memristive devices for neuromorphic applications: Comparative analysis," Bionanoscience **10**(4), 834–847 (2020).

[2] N. Zins, Y. Zhang, C. Yu, and H. An, "Neuromorphic computing: A path to artificial intelligence through emulating human brains," in *Frontiers of Quality Electronic Design (QED): AI, IoT and Hardware Security*, edited by A. Iranmanesh (Springer International Publishing, Cham, 2023), pp. 259–296.

[3] A. Emboras, A. Alabastri, P. Lehmann, K. Portner, C. Weilenmann, P. Ma, B. Cheng, M. Lewerenz, E. Passerini, U. Koch, J. Aeschlimann, F. Ducry, J. Leuthold, and M. Luisier, "Opto-electronic memristors: Prospects and challenges in neuromorphic computing," Appl. Phys. Lett. **117**(23), 230502 (2020).

[4] W. J. Duan, J. B. Wang, X. L. Zhong, H. J. Song, and B. Li, "Switchable Cu_2O/WO_X p–n junction for high density crossbar arrays," RSC Adv. **6**(104), 102603–102607 (2016).

[5] S. Lamichhane, S. Sharma, M. Tomar, and A. Chowdhuri, "Effect of annealing on resistive switching properties of glancing angle deposition-assisted WO_3 thin films," Phys. Status Solidi A **220**(20), 2300358 (2023).

[6] S. Kossar, R. Amiruddin, and A. Rasool, "Investigation on asymmetric resistive switching (RS) characteristics in p-NiO/n-ZnO heterojunctions," Microelectron. Eng. **254**, 111669 (2022).

[7] M. U. Khan, G. Hassan, and J. Bae, "Highly bendable asymmetric resistive switching memory based on zinc oxide and magnetic iron oxide heterojunction," J. Mater. Sci.: Mater. Electron. **31**(2), 1105–1115 (2020).

[8] F. Zahoor, T. Z. Azni Zulkifli, and F. A. Khanday, "Resistive random access memory (RRAM): An overview of materials, switching mechanism, performance, multilevel cell (MLC) storage, modeling, and applications," Nanoscale Res. Lett. **15**(1), 90 (2020).

[9] O. K. Prasad, S. Chandrasekaran, C. H. Chung, K. M. Chang, and F. M. Simanjuntak, "Annealing induced cation diffusion in TaO_x-based memristor and its compatibility for back-end-of-line post-processing," Appl. Phys. Lett. **121**(23), 233505 (2022).

02 July 2025 08:13:56

© Author(s) 2025

[10]P. Nonglen Meitei and N. K. Singh, "Effect of annealing on forming-free bipolar resistive switching of Gd_2O_3 thin films," J. Alloys Compd. **941**, 168900 (2023).
[11]S. Shrivastava, Y. T. Lin, B. Pattanayak, S. Pratik, C. C. Hsu, D. Kumar, A. S. Lin, and T. Y. Tseng, "Zn_2SnO_4 thin film based nonvolatile positive optoelectronic memory for nuromorphic computing," ACS Appl. Electron Mater. **4**(4), 1784–1793 (2022).
[12]Z. Shen, Y. Qi, I. Mitrovic, C. Zhao, S. Hall, L. Yang, T. Luo, Y. Huang, and C. Zhao, "Effect of annealing temperature for Ni/AlO_x/Pt RRAM devices fabricated with solution-based dielectric," Micromachines **10**(7), 446 (2019).
[13]C. C. Hsu, Y. S. Lin, C. W. Cheng, and W. C. Jhang, "Annealing effect on the performance of copper oxide resistive memory devices," IEEE Trans. Electron Devices **67**(3), 976–983 (2020).
[14]S. Biswas, A. D. Paul, C. Ghosh, A. Mondal, and R. Mahapatra, "Active electrode dependence of HfO_x-based flexible RRAM with a stack engineered thermal enhancement layer," IEEE Trans. Electron Devices **71**, 7470 (2024).
[15]S. Shrivastava, S. E. Limantoro, H. Juliano, and T. Y. Tseng, "Bidirectional photoelectric response of perovskite oxide-based synaptic ReRAM device," IEEE Electron Device Lett. **45**(3), 384–387 (2024).
[16]S. Shrivastava, H.-N. Chi, S. E. Limantoro, H. Juliano, and T.-Y. Tseng, "Fully visible light controlled neuro-synaptic ReRAM device based on metal oxide heterojunction," Appl. Phys. Lett. **124**(13), 133503 (2024).
[17]P.-Y. Chen, B. Lin, I.-T. Wang, T.-H. Hou, J. Ye, S. Vrudhula, J. Seo, Y. Cao, and S. Yu, "Mitigating effects of non-ideal synaptic device characteristics for on-chip learning," in *2015 IEEE/ACM International Conference on Computer-Aided Design (ICCAD)* (IEEE, 2015), pp. 194–199.
[18]S. Shrivastava, W. Dai, S. E. Limantoro, H. Juliano, and T. Tseng, "A violet-light-responsive ReRAM based on Zn_2SnO_4/Ga_2O_3 heterojunction as an Artificial synapse for visual sensory and in-memory computing," Adv. Electron Mater **11**, 2400527 (2024).
[19]W. Huang, X. Xia, C. Zhu, P. Steichen, W. Quan, W. Mao, J. Yang, L. Chu, and X. Li, "Memristive artificial synapses for neuromorphic computing," Nano-Micro Lett. **13**(1), 85 (2021).
[20]S. Song and L. F. Abbott, "Cortical development and remapping through spike timing-dependent plasticity," Neuron **32**(2), 339–350 (2001).
[21]P. Stoliar, H. Yamada, Y. Toyosaki, and A. Sawa, "Spike-shape dependence of the spike-timing dependent synaptic plasticity in ferroelectric-tunnel-junction synapses," Sci. Rep. **9**(1), 17740 (2019).
[22]S. H. Lee, D. Lutz, M. Mossalam, V. Y. Bolshakov, M. Frotscher, and J. Shen, "Presenilins regulate synaptic plasticity and mitochondrial calcium homeostasis in the hippocampal mossy fiber pathway," Mol. Neurodegener. **12**(1), 48 (2017).
[23]J.-T. Huang, A. Saleem, Y.-H. Poh, and T.-Y. Tseng, "HfON-based optoelectronic memristor for synaptic computing," IEEE Trans. Electron Devices **71**(1), 536–541 (2024).
[24]C.-C. Hsu, S. Shrivastava, S. Pratik, S. Chandrasekaran, and T.-Y. Tseng, "ZTO/MgO-Based optoelectronic synaptic memristor for neuromorphic computing," IEEE Trans. Electron Devices **70**(3), 1048–1054 (2023).
[25]T.-L. Tsai, H.-Y. Chang, F.-S. Jiang, and T.-Y. Tseng, "Impact of post-oxide deposition annealing on resistive switching in HfO_2-based oxide RRAM and conductive-bridge RAM devices," IEEE Electron Device Lett. **36**(11), 1146–1148 (2015).
[26]F. M. Simanjuntak, S. Chandrasekaran, D. Panda, S. Rajasekaran, C. Rullyani, G. Madhaiyan, T. Prodromakis, and T.-Y. Tseng, "Negative effect of cations out-diffusion and auto-doping on switching mechanisms of transparent memristor devices employing ZnO/ITO heterostructure," Appl. Phys. Lett. **118**(17), 173502 (2021).
[27]D. Panda, Y.-F. Hui, and T.-Y. Tseng, "Harnessing a WO_x-based flexible transparent memristor synapse with a hafnium oxide layer for neuromorphic computing," Nanoscale **16**(34), 16148–16158 (2024).
[28]S. Chandrasekaran, F. M. Simanjuntak, R. Aluguri, and T. Y. Tseng, "The impact of TiW barrier layer thickness dependent transition from electro-chemical metallization memory to valence change memory in ZrO_2-based resistive switching random access memory devices," Thin Solid Films **660**, 777–781 (2018).
[29]Y. Kang, T. Liu, T. Potnis, and M. K. Orlowski, "Composite Cu/VO and VO/Cu nanofilaments in Cu/Ta_2O_5/Pt devices," ECS Solid State Lett. **2**(7), Q54 (2013).
[30]A. Saleem, D. Kumar, A. Singh, S. Rajasekaran, and T. Y. Tseng, "Oxygen vacancy transition in HfO_x-based flexible, robust, and synaptic Bi-layer memristor for neuromorphic and wearable applications," Adv. Mater. Technol. **7**(7), 2101208 (2022).
[31]R. Fernow, "Periodic table of the elements," in *Introduction to Experimental Particle Physics*, edited by R. C. Fernow (Cambridge University Press, Cambridge, 1986), pp. 386–387.
[32]F. M. Simanjuntak, S. Chandrasekaran, B. Pattanayak, C.-C. Lin, and T.-Y. Tseng, "Peroxide induced volatile and non-volatile switching behavior in ZnO-based electrochemical metallization memory cell," Nanotechnology **28**(38), 38LT02 (2017).
[33]H. Ebbinghaus, "Memory: A contribution to experimental psychology," Ann. Neurosci. **20**(4), 155 (2013).
[34]S. K. Mehta, I. Mondal, B. Yadav, and G. U. Kulkarni, "Energy-efficient resistive switching synaptic devices based on patterned Ag nanotriangles with tunable gaps fabricated using plasma-assisted nanosphere lithography," Nanoscale **16**, 18365 (2024).
[35]C. S. Green and D. Bavelier, "Exercising your brain: A review of human brain plasticity and training-induced learning," Psychol. Aging **23**(4), 692–701 (2008).
[36]T. Ohno, T. Hasegawa, T. Tsuruoka, K. Terabe, J. K. Gimzewski, and M. Aono, "Short-term plasticity and long-term potentiation mimicked in single inorganic synapses," Nat. Mater. **10**(8), 591–595 (2011).
[37]R. C. Atkinson and R. M. Shiffrin, "Human memory: A proposed system and its control processes," Psychol. Learn. Motiv. **2**(C), 89–195 (1968).
[38]R. Jana, R. Bhunia, S. Paramanik, K. Giri, and A. Chowdhury, "Conductive islands assisted resistive switching in biomimetic artificial synapse for associative learning and image recognition," Adv. Funct. Mater. **35**, 2412804 (2024).
[39]F. Ma, Y. Zhu, Z. Xu, Y. Liu, X. Zheng, S. Ju, Q. Li, Z. Ni, H. Hu, Y. Chai, C. Wu, T. W. Kim, and F. Li, "Optoelectronic perovskite synapses for neuromorphic computing," Adv. Funct. Mater. **30**(11), 1908901 (2020).
[40]H. Widiyandari, I. Firdaus, V. G. S. Kadarisman, and A. Purwanto, "Optical properties and photocatalytic activities of tungsten oxide (WO_3) with platinum co-catalyst addition," AIP Conf. Proc. **1712**, 050027 (2016).
[41]A. T. Ravichandran, K. Dhanabalan, A. Vasuhi, R. Chandramohan, and S. Mantha, "Morphology, bandgap, and grain size tailoring in Cu_2O thin film by SILAR method," IEEE Trans. Nanotechnol. **14**(1), 108–112 (2015).
[42]Y. Fang, Q. Li, J. Meng, T. Wang, H. Zhu, Q.-Q. Sun, D. W. Zhang, and L. Chen, "Photonic synapses for image recognition and high density integration of simplified artificial neural networks," Adv. Electron. Mater. **9**(6), 2300120 (2023).

02 July 2025 08:13:56

© Author(s) 2025